

Article

Mo–Bi Bimetallic Chalcogenide Nanoparticles Supported on CNTs for the Efficient Electrochemical Reduction of CO₂ to Methanol

Chen Chi *, Donghong Duan, Zhonglin Zhang, Guoqiang Wei, Yu Li and Shibin Liu * 

College of Chemistry and Chemical Engineering, Taiyuan University of Technology, Taiyuan 030024, China; duandonghong@tyut.edu.cn (D.D.); zlzhang@tyut.edu.cn (Z.Z.); weiguoqiang@tyut.edu.cn (G.W.); liyu@tyut.edu.cn (Y.L.)

* Correspondence: chichen0058@link.tyut.edu.cn (C.C.); sbliu@tyut.edu.cn (S.L.)

Received: 6 October 2020; Accepted: 19 November 2020; Published: 24 November 2020



Abstract: The electrochemical reduction of CO₂ to methanol is a promising strategy, which currently suffers from the poor catalytic activity, selectivity, and stability of the electrode. Here, we report a simple one-pot hydrothermal strategy to fabricate Mo–Bi BMC@CNT nanocomposites, in which Mo–Bi bimetallic chalcogenide nanoparticles were in-situ decorated on carbon nanotubes. The Mo–Bi BMC nanoparticles with an average particle size of 12 nm were uniformly supported on the surface of CNTs without aggregation into larger clusters. The Mo–Bi BMC@CNT nanocomposites exhibited a relatively good catalytic performance for the electrochemical reduction of CO₂ to methanol in a 60 wt.% 1-ethyl-3-methylimidazolium tetrafluoroborate aqueous electrolyte. Among them, the Mo–Bi BMC@CNT-15% nanocomposite showed the highest Faradaic efficiency of 81% for methanol at –0.3 V vs. a saturated calomel reference electrode (SCE) and a stable current density is 5.6 mA cm^{–2} after a run time of 12 h. The excellent catalytic properties are likely attributed to its nanostructure and fast electron transfer. These derive from the synergistic effect of Mo–Bi and the high conductivity of CNTs. This work opens a way to provide an efficient catalytic system for the electroreduction of CO₂ to methanol in industrial applications.

Keywords: Mo–Bi bimetallic chalcogenide; CNTs; CO₂ electroreduction; methanol

1. Introduction

Carbon dioxide (CO₂) is a greenhouse gas for global climate change. However, it is a cheap and abundant carbon resource for useful chemicals and fuels [1]. The conversion of CO₂ into value-added products has received increasing attention because it is considered a promising strategy to reduce the greenhouse effect with significant economic and environmental benefits [2,3]. A variety of chemical, thermochemical, photochemical, electrochemical, and photoelectrochemical methods have been developed for CO₂ conversion [4]. Compared to other methods, great research efforts are currently investigating the electrochemical CO₂ reduction method [5–8]. Value-added products have been synthesized, including CO [8–11], formic acid/formate [12,13], methane [14,15], methanol [16], ethylene [17], etc.

Methanol is one of the most valuable products of electrochemical CO₂ reduction as it is not only an excellent fuel in internal combustion engines but also a cheap feedstock for the production of light olefins [18–20]. However, some challenges exist in large-scale electrochemical CO₂ reduction. The critical bottleneck is the low electrochemical efficiency of CO₂ reduction to methanol. The hydrogen evolution reaction (HER) and CO₂ reduction reaction (CO₂RR) are competitive reactions in kinetics [21,22].

To improve the low electrochemical efficiency and reduce the effects of the hydrogen evolution reaction, there are intensive investigations are to find highly active, selective, and stable electrocatalytic systems by optimizing different parameters, including the electrode materials, electrolytes, and applied overpotentials. The typical electrocatalysts, containing single metals, alloys, metal oxides, and transition-metal chalcogenides, have been used to convert CO₂ selectively to methanol in different electrolytes [23–25]. Among them, molybdenum disulfide (MoS₂), as an efficient catalyst for CO₂ reduction, has attracted more attention due to the unique mechanical, electrical, and optical properties.

Asadi et al. reported that the electrocatalytic activity of MoS₂ is mainly from the edge exposed Mo atoms that reduce the free energy of CO₂ conversion [24]. However, MoS₂ exhibited low selectivity with relatively high overpotentials. Therefore, the hetero atom doping, hybridization, composition, and surface modification of MoS₂ were efficient strategies to enhance the electronic structures and edge-exposed active sites, which usually led to a significant improvement of the CO₂RR and a suppression of the HER [25].

For instance, Han et al. synthesized a Mo–Bi metallic chalcogenide electrocatalyst using a one-pot solvothermal reaction, which was used for CO₂ electroreduction to methanol. This catalyst exhibited high methanol selectivity (Faradaic efficiency of methanol reached 71.2%), a low reaction overpotential (360 mV), and high current density (−12.1 mA·cm^{−2} at −0.7 V vs. Standard hydrogen electrode (SHE)) [26]. Li et al. synthesized a hierarchical hollow catalyst using N-doped carbon and edge-exposed 2H–MoS₂ (NCMSH) for CO₂RR. This catalyst showed high CO Faradaic efficiency up to 90.2% and a low overpotential of 130 mV for CO formation. These results indicate that NCMSH displayed superior catalytic activity compared with E–MoS₂ and other transition metal sulfides [27].

In this paper, we constructed Mo–Bi BMC@CNTs electrocatalysts for the first time via a one-pot hydrothermal reaction with exposed Mo and Bi atoms on the surface of CNTs. The electrocatalysts with different CNT contents were investigated for CO₂ electroreduction to methanol. The electrochemical tests demonstrated that the CNTs supports improved the conductivity and provided a direct electron transfer pathway, thereby, enhancing the catalytic performance for the CO₂ electroreduction to methanol. This work offers an efficient electrode for the electrochemical reduction of CO₂ to methanol, which exhibits a promising potential in industrial applications.

2. Experimental Details

2.1. Materials

Ammonium tetrathiomolybdate ((NH₄)₂MoS₄, 99.95%), bismuth nitrate pentahydrate (Bi(NO₃)₃·5H₂O), and carbon dioxide gas with a purity of 99.999% were purchased from Sinopharm Group Shanxi Co., Ltd, Taiyuan, China. The carbon nanotubes (D: 30–50 nm, L: 0.5–2 μm) were purchased from Nanjing XFNANO Materials Tech Co., Ltd., Nanjing, China. 1-Ethyl-3-methylimidazolium tetrafluoroborate ([Emim]BF₄, purity > 99%) was purchased from Shanghai Cheng Jie Chemical Co., Ltd., Shanghai, China. Nafion N-117 membrane and Nafion D-521 dispersion (5 wt.%) were purchased from Alfa Aesar China Co., Ltd., Shanghai, China.

2.2. Synthesis of Mo–Bi BMC Nanoparticles

First, 0.10 g (NH₄)₂MoS₄ and 0.19 g Bi(NO₃)₃·5H₂O were dissolved in 40 mL of deionized water with 30 min of magnetic stirring. Then, the solution was shifted into a 50 mL autoclave and heated at different temperatures (185, 200, 215, and 230 °C) for 12 h. After cooling to room temperature, the black precipitate was centrifuged and washed with mono-ethanolamine and deionized water for three times. Finally, the final product was vacuum dried.

2.3. Synthesis of Mo–Bi BMC@CNTs

The functionalized CNTs with a carboxylic acid group were obtained by a heating reflux (110 °C) of CNTs in a mixture of HNO₃ and H₂SO₄ (1:3) for 2 h. The Mo–Bi BMC@CNTs nanocomposites

were also synthesized by a similar hydrothermal procedure at 200 °C for 12 h in the presence of the functionalized CNTs.

2.4. Materials Characterization

X-ray diffraction (XRD) patterns were obtained on a diffraction meter (RIGAKU 3KW D/MAX-2200 V/PC, Tokyo, Japan) with Cu-K α radiation. Scanning electron microscope (SEM) images were taken on a field emission scanning electron microscopy (S-4800, HITACHI, Tokyo, Japan) operating at 15 kV. Transmission electron microscope (TEM) images were acquired using a transmission electron microscope (JEM-2010, JEOL, Tokyo, Japan) operated at 200 kV. The composition and chemistry of the incorporated solid were examined by X-ray photoelectron spectroscopy (XPS, Thermo Scientific ESCALAB 250Xi-XL, Birmingham, UK) using Al-K α radiation, and the binding energies were calculated with respect to C 1s at 284.8 eV and measured with a precision of ± 0.05 eV.

2.5. Electrochemical Study

To prepare the working electrode, 2 mg catalyst material was dispersed in 1 mL ethanol with 50 μ L Nafion D-521 dispersion (5 wt.%) to form a uniform suspension by ultrasound. Then, 10 μ L of the ink was coated on the glassy carbon electrode (CP φ = 6 mm) surface using a micropipette and dried under an infra-red (IR) lamp. The loading of the Mo–Bi BMC catalyst was 0.07 mg cm $^{-2}$.

All of the experiments of CO $_2$ reduction were tested through an electrochemical workstation (Princeton, VMP3, Lyon, France). Linear sweep voltammetry (LSV) and chronoamperometry (CA) tests were conducted in a H-type cell with a three-electrode configuration, which consisted of a working electrode (CP electrode), a platinum gauze auxiliary electrode, and a saturated calomel reference electrode (SCE).

In the H-type cell, 60 wt.% [Emim] BF $_4$ aqueous electrolyte was used as the cathode electrolyte, and H $_2$ SO $_4$ aqueous solution (0.5 M) was used as the anode electrolyte. The cathode and anode compartments were separated by a Nafion 117 proton exchange membrane.

The electrolyte was bubbled with Ar or CO $_2$ for at least 30 min to form an Ar or CO $_2$ saturated solution with slight magnetic stirring before electrolysis. The LSV measurements in the gas-saturated electrolyte were conducted in the potential range of 0 to -0.5 V vs. SCE at a sweep rate of 5 mV \cdot s $^{-1}$. Then, the chronoamperometry (CA) test was carried out with CO $_2$ bubbling with the flow rate controlled at 2 mL/min.

2.6. Product Analysis

The gaseous products of electrochemical experiments were collected once an hour using a gas bag and analyzed with gas chromatography (GC, Haixin 950 N, Shanghai, China), which was equipped with flame ionization detector (FID) and thermal conductivity detector (TCD) using Ar as the internal standard. After the CA test, the liquid products were collected by fractionation at 100 °C and analyzed using GC.

The Faradaic efficiency (FE) of CO $_2$ reduction products was calculated using the following equation:

$$FE = \frac{z \times n \times F}{\sum It}, \quad (1)$$

where n is the number of moles of methanol formed as determined by GC, F is the Faraday constant, z is the number of electrons involved in the products formation reaction (such as for the conversion of CO $_2$ to methanol, z is 6), I is the total current, and t is the time.

3. Results and Discussion

3.1. XRD Patterns of the Mo–Bi BMC and Mo–Bi BMC@CNTs

The corresponding XRD patterns of Mo–Bi BMC nanoparticles synthesized at different hydrothermal temperature are shown in Figure 1a. The XRD patterns reveal that all diffraction peaks matched well with the standard pattern of MoS₂ (JCPDS card No. 17-0744) and Bi₂S₃ (JCPDS card No.17-0320), respectively [28]. When Mo–Bi BMC nanomaterials were synthesized at 185 °C, only certain broadened characteristic diffraction peaks at 24.93° and 28.06° were observed, corresponding to the (130) and (211) crystal plane of Bi₂S₃.

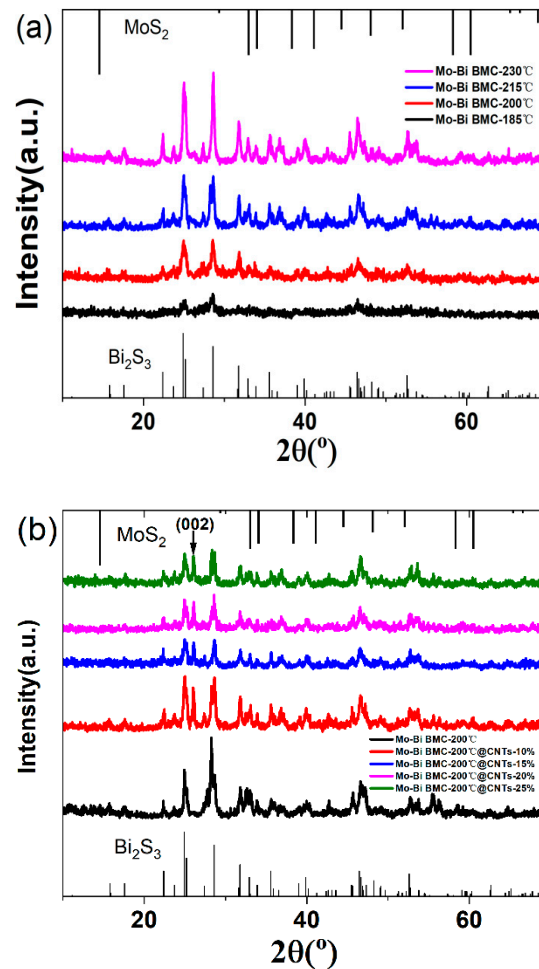


Figure 1. X-ray diffraction (XRD) patterns of the (a) Mo–Bi BMC, and (b) Mo–Bi BMC@CNTs.

With the temperature increased from 200 to 230 °C, the 33.03° and 34.06° diffraction peaks appeared in the XRD patterns, corresponding to the (101) and (012) crystal plane of MoS₂. With the increase of temperature, more diffraction peaks appeared and became more intensive and sharper, implying a good crystalline structure of the Mo–Bi BMC nanomaterials. This demonstrates that the Bi₂S₃ appeared even at 185 °C and that a mixed-phase of MoS₂ and Bi₂S₃ was formed above 200 °C. The Mo–Bi BMC nanoparticles synthesized at 200 °C were found to be the smallest crystal size, which was calculated using the Scherrer formula [29].

Figure 1b shows the XRD patterns of the Mo–Bi BMC@CNTs nanocomposites with different CNT contents. The diffraction peak of the CNTs were located at $2\theta = 26.3^\circ$, which can be assigned to the hexagonal (002) crystal planes of the graphite [30]. The intensities of the other diffraction peaks

gradually increased with the elevated CNT content. All the results indicated that these Mo–Bi BMC and CNTs components were fully compounded together.

We calculated and compared the crystallite size using XRD data, the results are shown in Table 1.

Table 1. Crystallite size of the catalysts calculated using the XRD data.

Sample	2 θ	Peak	Crystallite Size
Mo–Bi BMC-185 °C	28.06°	(2 1 1)	13.03 nm
Mo–Bi BMC-200 °C	28.04°	(2 1 1)	12.16 nm
Mo–Bi BMC-215 °C	28.07°	(2 1 1)	12.25 nm
Mo–Bi BMC-230 °C	28.06°	(2 1 1)	12.57 nm
Mo–Bi BMC-200 °C@ CNTs-10%	28.03°	(2 1 1)	7.81 nm
Mo–Bi BMC-200 °C@ CNTs-15%	28.05°	(2 1 1)	7.57 nm
Mo–Bi BMC-200 °C@ CNTs-20%	28.06°	(2 1 1)	7.59 nm
Mo–Bi BMC-200 °C@ CNTs-25%	28.08°	(2 1 1)	7.63 nm

3.2. SEM Images of the Mo–Bi BMC and Mo–Bi BMC@CNTs

The SEM images of the Mo–Bi BMC nanoparticles are shown in Figure 2. The morphologies of Mo–Bi BMC nanoparticles changed with the reaction temperature. The nanoparticles synthesized at 185 °C showed a nanofiber form, which slowly turned into particles when synthesized at above 200 °C. The Mo–Bi BMC nanoparticles showed that the agglomerations of particles were much less.

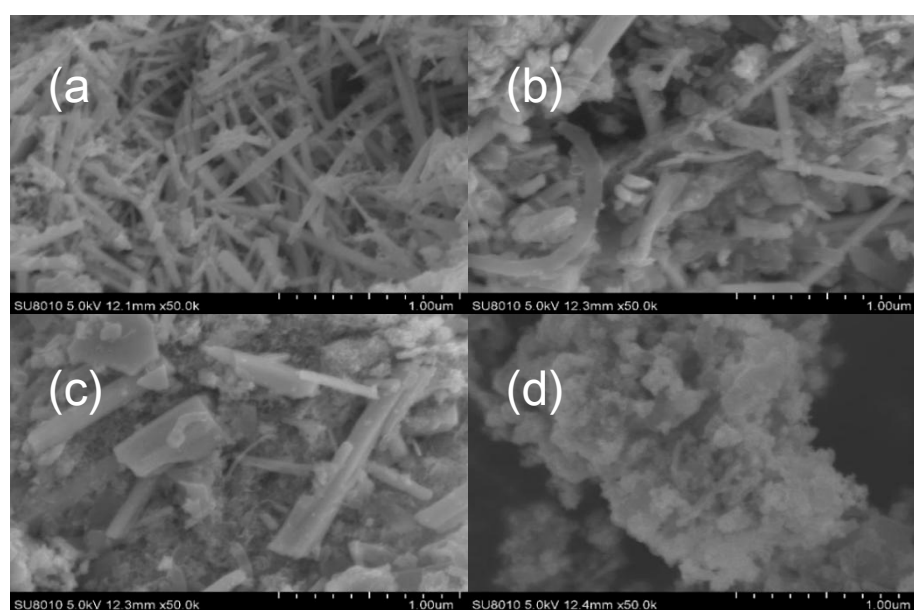


Figure 2. Scanning electron microscope (SEM) images of the Mo–Bi BMC nanoparticles synthesized at different hydrothermal temperatures: (a) 185 °C, (b) 200 °C, (c) 215 °C, and (d) 230 °C.

Figure 3 shows SEM images of the Mo–Bi BMC@CNT nanocomposites with different CNT contents. The nanocomposites consist of a tubular structure of CNTs and irregular agglomeration of particles. The density of the agglomerated particles decreased with the increase in the CNT contents. As shown in Figure 3c, when the CNT content increased to 25%, the diameter of tubular structure was about 103 nm, larger than the pure CNTs with a diameter of 30–50 nm. This indicates that the Mo–Bi BMC nanoparticles were highly dispersed over the entire surface of the CNTs to form a network structure [31].

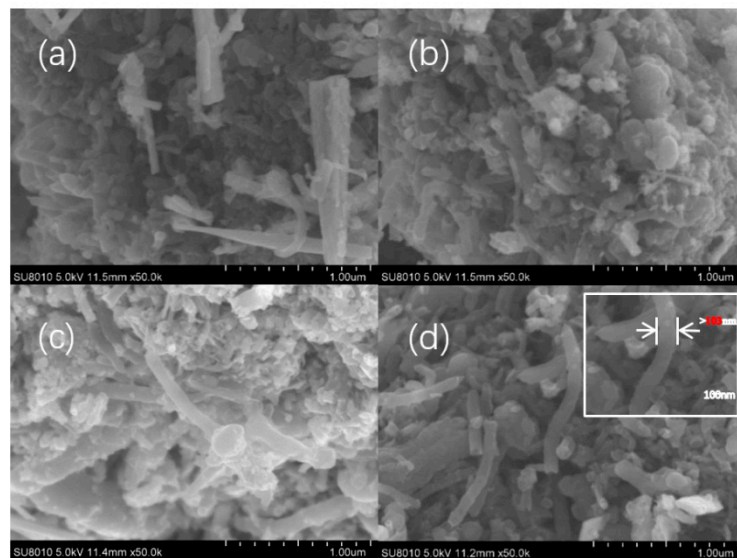


Figure 3. SEM images of the Mo–Bi BMC@CNTs nanocomposites with different CNT contents (a) 10%, (b) 15%, (c) 20%, (d) 25%.

3.3. TEM Images of the Mo–Bi BMC and Mo–Bi BMC@CNTs

TEM images were used to further examine the morphologies of Mo–Bi BMC-200 °C and Mo–Bi BMC@CNTs-15% nanocomposites, as shown in Figure 4. The pure Mo–Bi BMC-200 °C particle size was uniform and around 20 nm with aggregation as shown in Figure 4b. The Mo–Bi BMC nanoparticles of the nanocomposite were uniformly anchored and directly grew on the CNTs surface in Figure 4c. The particle size of Mo–Bi BMC decreased to 12 nm in the presence of the CNTs-15%. The average particle size obtained by TEM was close to the crystallite size calculated from the XRD results. The dispersion of small particles is optimal for surface catalysis as this can provide more active sites for the reactants.

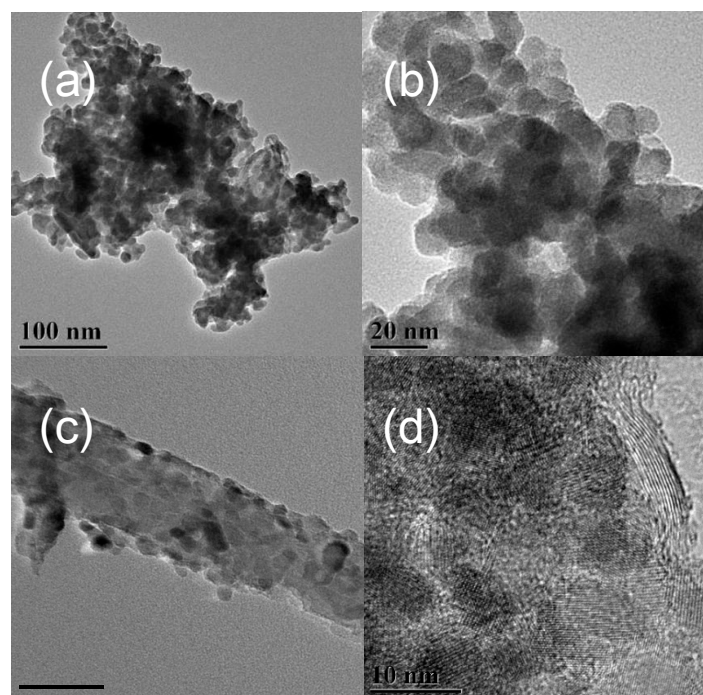


Figure 4. Transmission electron microscope (TEM) images of the Mo–Bi BMC-200 °C (a,b) and Mo–Bi BMC@CNTs-15% (c,d) nanocomposites.

The chemical bonding and elemental electronic states were further investigated using XPS. The characteristic peaks belonging to Mo^{4+} ($\text{Mo } 3d_{3/2}$: 235.3 and 232.9 eV; $\text{Mo } 3d_{5/2}$: 231.8 and 228.6 eV), Bi^{3+} ($\text{Bi } 4f_{5/2}$: 164.2 and 159.4 eV; $\text{Bi } 4f_{7/2}$: 163.7 and 158.3 eV), and S ($\text{S } 2s$: 225.6 eV; $\text{S } 2p$: 161.3 and 162.6 eV) were detected from the spectra. The results confirmed that the nanocomposites were composed of MoS_2 and Bi_2S_3 . The binding energy of $\text{Mo } 3d$ and $\text{Bi } 4f$ peaks shifted lower compared to the standard MoS_2 and Bi_2S_3 peaks, which further proved that there was a strong interaction between MoS_2 and Bi_2S_3 [26,32]. The XPS results also showed the atomic percent of Mo and Bi as shown in Table 2, which help prove that the ratio of Mo and Bi was nearly 1:1.

Table 2. X-ray photoelectron spectroscopy (XPS) peaks table.

Name	FWHM eV	Area (P) CPS.eV	Area (N) TPP-2M	Atomic %
C 1s	1.81	30,611.72	0.7	75.4
Mo 3d	2	20,229.59	0.04	4.47
Bi 4f7 Scan A	1.36	29,915.32	0.03	3.35
Bi 4f7 Scan B	1.32	7831.45	0.01	0.88
S 2p3	1.34	4122.18	0.07	7.95
S 2p1	1.34	2105.65	0.07	7.95

3.4. Electrochemical Performances of the Mo–Bi BMC and Mo–Bi BMC@CNTs

The electrocatalytic CO_2RR activity of the prepared electrodes (Mo–Bi BMC and Mo–Bi BMC@CNTs) were measured by linear sweep voltammetry in 60 wt.% [Emim] BF_4 aqueous electrolyte as shown in Figure 5. Generally, only the HER occurred in the Ar-saturated electrolyte, but both the HER and CO_2RR occurred in the CO_2 -saturated electrolyte [33,34]. The current density of the CO_2RR was higher than that of the HER, which indicates the catalytic efficacy of the electrode toward the CO_2RR . Figure 5a shows the linear sweep voltammetry of Mo–Bi BMC synthesized with different temperatures in the CO_2 saturated electrolyte.

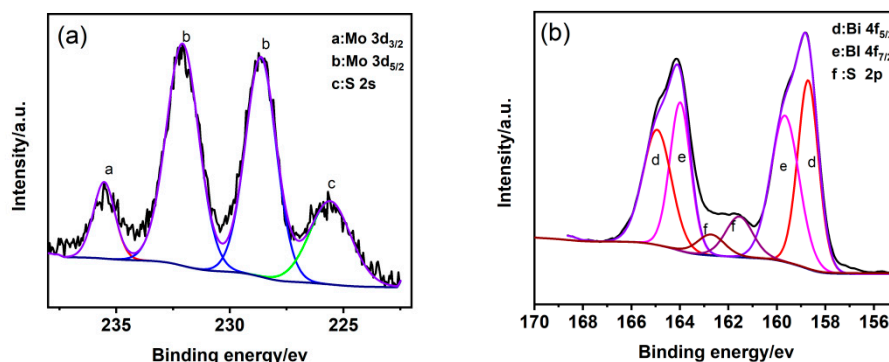


Figure 5. XPS spectra orbits of the Mo–Bi BMC-15% Nanocomposites. (a) Mo 3d and S 2s, (b) Bi 4f and S 2p.

We observed a significant increase of the cathodic current density, which could be attributed to the CO_2RR in addition to the HER. The Mo–Bi BMC-200 °C showed the highest CO_2RR current (11.3 mA cm^{-2}) at around -0.5 V . This indicates that the Mo–Bi BMC-200 °C had a clear catalytic activity for the CO_2RR . A likely reason is the excellent synergistic effect of Mo and Bi.

In the presence of [Emim] BF_4 , the Bi sites can effectively promote surface-adsorbed C–O (C–O_{ads}) intermediates, and the edge exposed Mo atoms are favorable for producing H_2 . Mo atom sites can bind with C–O_{ads} , which promote the reduction from C–O_{ads} to methanol [35]. When Mo–Bi BMC was supported on CNTs, their performance was further improved under the same conditions (Figure 5b). The highest current density reached 16.2 mA cm^{-2} at -0.5 V vs. SCE for an optimal CNT content of

15%. Mo–Bi BMC@CNTs not only offer more active sites but also trap electrons to increase the rate of conversion of the C–O intermediates to methanol [36].

The electrocatalytic selectivity of the Mo–Bi BMC and Mo–Bi BMC@CNTs electrodes were further detected by CA experiments at the variable applied potential. Based on the previous reported studies, methanol was detected to be the predominant liquid product from CO₂ reduction. The Faradaic efficiency of methanol was plotted as a function of the applied potential as shown in Figure 6. The fact that the Faradaic efficiency value was significantly less than 100% suggests that other reduction products are present, which were determined to be CO, H₂, and CH₄.

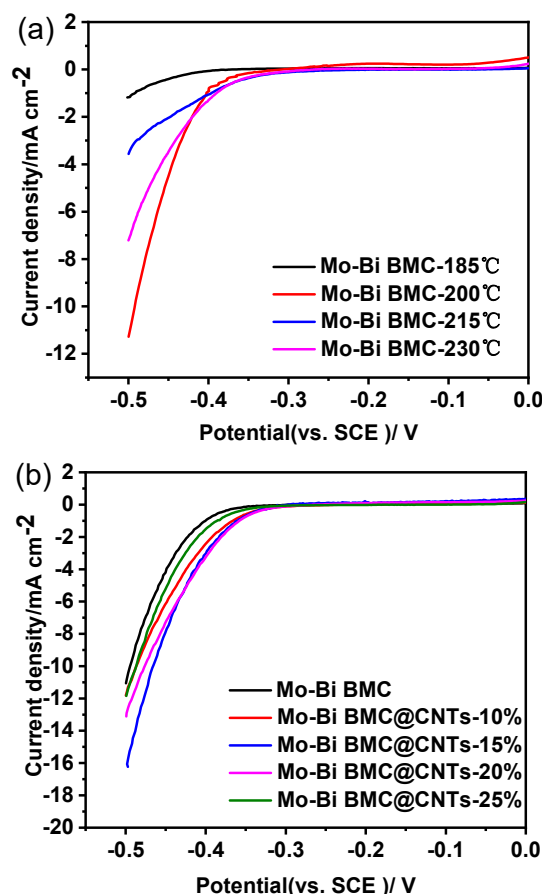


Figure 6. Linear sweep voltammetry of the Mo–Bi BMC (a) and Mo–Bi BMC@CNTs (b).

From Figure 6a, the Faradaic efficiency for methanol was found to increase quickly with the applied potential for all electrodes, reaching a maximum value at -0.3 V vs. SCE. Then the Faradaic efficiency decreased slightly at a more negative potential, which was likely caused by the mass transport limitations of CO₂ in the solution. Mo–Bi BMC-200 °C gave a relatively high Faradaic efficiency for methanol over a broad range of potential suggesting that it was highly selective toward methanol. At an applied potential of -0.3 V vs. SCE, methanol was generated with its maximum Faradaic efficiency of 46% using the Mo–Bi BMC electrode.

The high catalytic selectivity of the Mo–Bi BMC electrode can be attributed to the synergistic effect between the Mo and Bi atom for producing methanol. As CO and H₂ can be produced on the electrode, the CO is bound and can be further hydrogenated to methanol. As CO_{ads} and H₂ can be simultaneously produced on the catalyst, the CO_{ads} can also be further hydrogenated to produce methanol [37].

According to the literature, the presence of highly-conductive CNTs increases the electronic conductivity. Therefore, the charge transfer resistance is reduced and the charge density is increased, leading to a faster electron transfer rate from the catalysts to CO₂ [34–36]. As shown in Figure 7,

when Mo–Bi BMC was loaded onto CNTs, the Faradaic efficiency for methanol was further improved under the same conditions.

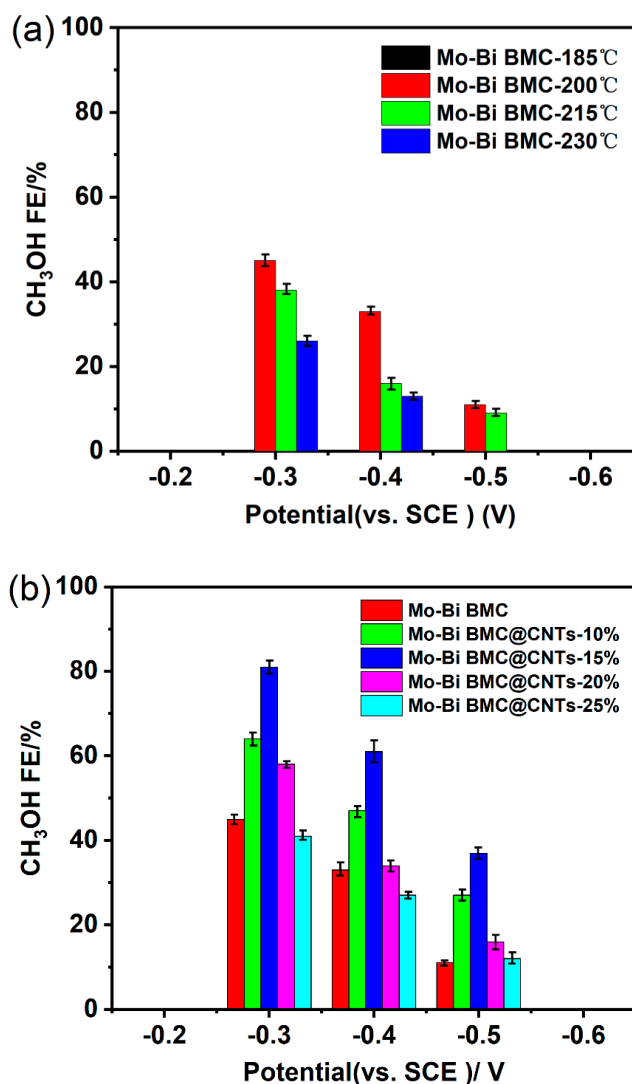


Figure 7. Faradaic efficiencies of methanol in the CO₂RR over the Mo–Bi BMC (a) and Mo–Bi BMC@CNTs (b) as a function of the potentials.

The Mo–Bi BMC@CNTs-15% catalyst exhibited the highest Faradaic efficiency for methanol production of 81% at -0.3 V vs. SCE. These values are in good agreement with the results shown in Figure 5, where the Mo–Bi BMC@CNTs electrode possessed a higher current density compared to the Mo–Bi BMC electrode. As far as we are aware, the excellent performance of the Mo–Bi BMC@CNTs electrode is slightly higher than any other known methanol-producing CO₂RR electrocatalysts in the reported literature (In Table 1). This is likely due to benefiting from its nanostructure and fast electron transfer as shown in Figure 2.

To evaluate the durability of the Mo–Bi BMC-200 °C and Mo–Bi BMC@CNT electrodes, the CA experiment was conducted with an applied potential of -0.3 V over 12 h (Figure 8). Both Mo–Bi BMC-200 °C and Mo–Bi BMC@CNTs electrodes exhibited excellent stability over 12 h of operation without any obvious degradation in the partial current density of methanol. The current density based on the substrate geometric area for Mo–Bi BMC@CNTs was approximately two times higher than that of Mo–Bi BMC-200 °C, which is likely attributed to the strong anchoring effect between the active Bi–Mo structure and the CNTs. This further indicates that CNTs supported Mo–Bi BMC could successfully improve the catalytic performance.

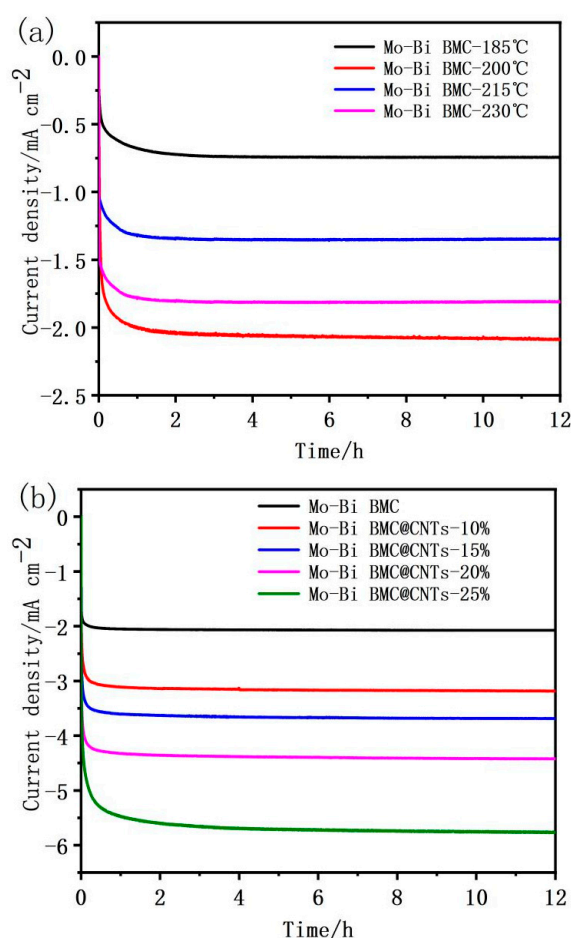


Figure 8. A 12 h long-term CA at -0.30 V over Mo-Bi BMC (a) and Mo-Bi BMC@CNTs (b).

We summarized current research work on the preparation of methanol by electrocatalytic reduction of CO_2 and the results are shown in Table 3.

Table 3. The Faradaic efficiency (FE) of methanol and the current density (CD) in CO_2 reduction using various electrodes and electrolytes. Saturated calomel reference electrode (SCE), Reversible hydrogen electrode (RHE).

Electrode/Electrocatalysts	Electrode Potential/V	Electrolyte	FE/%	CD/ mA cm^{-2}	Reference
Mo-Bi BMC@CNTs	-0.3 V vs. SCE	60 wt.% [Emim] BF_4 aqueous electrolyte	81	5.6	This work
Mo-Bi BMC	-0.3 V vs. SCE	60 wt.% [Emim] BF_4 aqueous electrolyte	46	2.1	This work
co-protoporphyrin/pyrolytic graphite electrode	-0.5 V vs. RHE	0.5 M KHCO_3	38	Not mentioned	[10]
Mo-Bi BMC nanosheet	-0.7 V vs. SHE	0.5 M [Bmim] BF_4 in MeCN	71.2	12.1	[26]
Mo	-0.7 V vs. SCE	0.2 M Na_2SO_4 (aq)	55	0.05	[26]
carbon paper/ Cu_2O	-1.3 V vs. Ag/AgCl	0.5 M KHCO_3	45.7	6.93	[38]
$\text{Cu}_2\text{O}/\text{ZnO}$ and pyridine-based cocatalyst	-0.8 V vs. Ag/AgCl	10 mM 2-mPy	25.6	10	[39]
$\text{Cu}_2\text{O}/\text{TiO}_2$	-0.7 V vs. RHE	0.5 M KHCO_3	53.6	1.3	[40]
ZnO@ZnTe@CdTe nanorod	-0.3 V vs. RHE	0.5 M KHCO_3	74.9	3.88	[41]
TiO_2 -protected InP nanopillars	-0.6 V vs. NHE	0.5 M NaHCO_3	8.7	Not mentioned	[42]

4. Conclusions

In summary, Mo–Bi BMC@CNTs were fabricated using a one-pot hydrothermal strategy. Their particle sizes could be effectively tuned and uniformly dispersed on the surface of CNTs. The Mo–Bi BMC@CNTs exhibited excellent catalytic performance for the electrochemical reduction of CO₂ to methanol in a [Emim] BF₄ aqueous electrolyte. The Faradaic efficiency for the CO₂ electrochemical reduction to methanol was shown to be as high as 81% with a stable current density of 5.6 mA·cm⁻².

The excellent selectivity of the Mo–Bi BMC/CNTs electrode can be ascribed to the excellent synergistic effect between Mo and Bi and highly conductive CNTs for producing methanol. The Bi sites promote the generation from CO₂ to CO_{ads}, and the Mo atoms favor the formation of H₂. Then the CO_{ads} is bound with H₂ and can be further reduced to produce methanol. Thus, the methanol is likely generated by this reaction process: CO₂^{+e}→CO_{ads}^{+e,+H₂}→CH₃OH. This work provides an efficient electrocatalysis strategy to produce methanol from CO₂.

Author Contributions: Conceptualization, C.C. and S.L.; experiment and data processing, C.C.; reagents/materials/analysis tools D.D., Z.Z., G.W., and Y.L.; writing—original draft preparation, C.C.; writing—original draft preparation, S.L. All authors have read and agreed to the published version of the manuscript.

Funding: This research was funded by National Natural Science Foundation of China (21776191, 20676088).

Conflicts of Interest: The authors declare no conflict of interest.

References

1. Wentuan, B.; Wu, C.Z.; Xie, Y. Atomically thin two-dimensional solids: An emerging platform for CO₂ electroreduction. *ACS Energy Lett.* **2018**, *3*, 624–633. [[CrossRef](#)]
2. Zhuang, T.T.; Pang, Y.; Liang, Z.Q.; Wang, Z.Y.; Li, Y.; Tan, C.S.; Li, J.; Luna, P.D. Copper nanocavities confine intermediates for efficient electrosynthesis of C3 alcohol fuels from carbon monoxide. *Nat. Catal.* **2018**, *1*, 421. [[CrossRef](#)]
3. Birdja, Y.Y.; Perezgallent, E.; Figueiredo, M.C.; Gottle, A.J.; Calle-Vallejo, F.; Koper, M.T. Advances and challenges in understanding the electrocatalytic conversion of carbon dioxide to fuels. *Nat. Energy* **2019**, *4*, 732–745. [[CrossRef](#)]
4. Lewis, N.S.; Nocera, D.G. Powering the planet: Chemical challenges in solar energy utilization. *Proc. Natl. Acad. Sci. USA* **2006**, *103*, 15729–15735. [[CrossRef](#)]
5. Ting, L.R.L.; Yeo, B.S. Recent advances in understanding mechanisms for the electrochemical reduction of carbon dioxide. *Curr. Opin. Electrochem.* **2018**, *8*, 126–134. [[CrossRef](#)]
6. Glasing, J.P.; Champagne, M.F. Cunningham, graft modification of chitosan, cellulose and alginate using reversible deactivation radical polymerization (RDRP). *Green Sustain. Chem.* **2016**, 15–21. [[CrossRef](#)]
7. Whipple, D.T.; Kenis, P.J.A. Prospects of CO₂ utilization via direct heterogeneous electrochemical reduction. *J. Phys. Chem. Lett.* **2010**, *1*, 3451–3458. [[CrossRef](#)]
8. Rosen, B.A.; Salehikhajin, A.; Thorson, M.R.; Zhu, W.; Whipple, D.T.; Kenis, P.J.A.; Masel, R.I. Ionic liquid-mediated selective conversion of CO₂ to CO at low overpotentials. *Science* **2011**, *334*, 643–644. [[CrossRef](#)]
9. Dimeglio, J.L.; Rosenthal, J. Selective conversion of CO₂ to CO with high efficiency using an inexpensive bismuth-based electrocatalyst. *J. Am. Chem. Soc.* **2013**, *135*, 8798–8801. [[CrossRef](#)]
10. Shen, J.; Kortlever, R.; Kas, R.; Birdja, Y.Y.; Diazmorales, O.; Kwon, Y.; Ledezmayanez, I.; Schouten, K.J.P.; Mul, G.; Koper, M.T.M. Electrocatalytic reduction of carbon dioxide to carbon monoxide and methane at an immobilized cobalt protoporphyrin. *Nat. Commun.* **2015**, *6*, 8177. [[CrossRef](#)]
11. Wang, Y.X.; Niu, C.; Zhu, Y. Copper–silver bimetallic nanowire arrays for electrochemical reduction of carbon dioxide. *Nanomaterials* **2019**, *9*, 173. [[CrossRef](#)] [[PubMed](#)]
12. Hollingsworth, N.; Taylor, S.F.R.; Galante, M.T.; Jacquemin, J.; Longo, C.; Holt, K.B.; de Leeuw, N.H.; Hardacre, C. Reduction of carbon dioxide to formate at low overpotential using a superbase ionic liquid. *Angew. Chem.* **2015**, *54*, 14164–14168. [[CrossRef](#)] [[PubMed](#)]

13. Kang, X.C.; Zhu, Q.G.; Sun, X.F.; Hu, J.Y.; Zhang, J.L.; Liu, Z.M.; Han, B.X. Highly efficient electrochemical reduction of CO₂ to CH₄ in an ionic liquid using a metal–organic framework cathode. *Chem. Sci.* **2016**, *7*, 266–273. [[CrossRef](#)] [[PubMed](#)]
14. Manthiram, K.; Beberwyck, B.J.; Alivisatos, A.P. Enhanced electrochemical methanation of carbon dioxide with a dispersible nanoscale copper catalyst. *J. Am. Chem. Soc.* **2014**, *136*, 13319–13325. [[CrossRef](#)] [[PubMed](#)]
15. Kuhl, K.P.; Hatsukade, T.; Cave, E.R.; Abram, D.N.; Kibsgaard, J.; Jaramillo, T.F. Electrocatalytic conversion of carbon dioxide to methane and methanol on transition metal surfaces. *J. Am. Chem. Soc.* **2014**, *136*, 14107–14113. [[CrossRef](#)] [[PubMed](#)]
16. Hui, S.R.; Shaigan, N.; Neburchilov, V.; Zhang, L.; Malek, K.; Eikerling, M.; Luna, P.D. Three-dimensional cathodes for electrochemical reduction of CO₂: From macro to nano-engineering. *Nanomaterials* **2020**, *10*, 1884. [[CrossRef](#)] [[PubMed](#)]
17. Qiao, J.L.; Liu, Y.Y.; Zhang, J.J. A review of catalysts for the electroreduction of carbon dioxide to produce low-carbon fuels. *Chem. Soc. Rev.* **2014**, *43*, 631–675. [[CrossRef](#)]
18. Graciani, J.; Mudiyansele, K.; Xu, F.; Baber, A.E.; Evans, J.; Senanayake, S.D.; Stacchiola, D.J.; Liu, P.; Hrbek, J.; Sanz, J.F.; et al. Highly active copper-ceria and copper-ceria-titania catalysts for methanol synthesis from CO₂. *Science* **2014**, *345*, 546–550. [[CrossRef](#)]
19. Studt, F.; Sharafutdinov, I.; Abildpedersen, F.; Elkjaer, C.F.; Hummelshøj, J.S.; Dahl, S.; Chorkendorff, I.; Nørskov, J.K. Discovery of a Ni-Ga catalyst for carbon dioxide reduction to methanol. *Nat. Commun.* **2014**, *6*, 320–324. [[CrossRef](#)]
20. Centi, G.; Perathoner, S. Opportunities and prospects in the chemical recycling of carbon dioxide to fuels. *Catal. Today* **2009**, *148*, 191–205. [[CrossRef](#)]
21. Omae, I. Recent developments in carbon dioxide utilization for the production of organic chemicals. *Coord. Chem. Rev.* **2012**, *256*, 1384–1405. [[CrossRef](#)]
22. Costentin, C.; Robert, M.; Savéant, J.-M. Catalysis of the electrochemical reduction of carbon dioxide. *Chem. Soc. Rev.* **2013**, *42*, 2423–2436. [[CrossRef](#)] [[PubMed](#)]
23. Cadena, C.; Anthony, J.L.; Shah, J.K.; Brennecke, J.F. Why is CO₂ so soluble in imidazolium-based ionic liquids? *J. Am. Chem. Soc.* **2004**, *126*, 5300–5308. [[CrossRef](#)] [[PubMed](#)]
24. Asadi, M.; Kumar, B.; Behranginia, A.; Rosen, B.A.; Baskin, A.; Reprin, N.; Pisasale, D.; Phillips, P.; Zhu, W.; Haasch, R.; et al. Robust carbon dioxide reduction on molybdenum disulphide edges. *Nat. Commun.* **2014**, *5*, 4470–4478. [[CrossRef](#)]
25. Summers, D.P.; Leach, S.; Frese, K.W. The electrochemical reduction of aqueous carbon dioxide to methanol at molybdenum electrodes with low overpotentials. *J. Electroanal. Chem. Interfacial Electrochem.* **1986**, *205*, 219–232. [[CrossRef](#)]
26. Sun, X.F.; Zhu, Q.G.; Kang, X.C.; Liu, H.Z.; Qian, Q.L.; Zhang, Z.F.; Han, B.X. Molybdenum-Bismuth bimetallic chalcogenide nanosheets for highly efficient electrocatalytic reduction of carbon dioxide to methanol. *Angew. Chem.* **2016**, *55*, 6771–6775. [[CrossRef](#)]
27. Li, H.Y.; Liu, X.Z.; Chen, S.M.; Yang, D.R.; Zhang, Q.; Song, L.; Xiao, H.; Zhang, Q.H.; Gu, L.; Wang, X. Edge-exposed molybdenum disulfide with N-doped carbon hybridization: A hierarchical hollow electrocatalyst for carbon dioxide Reduction. *Adv. Energy Mater.* **2019**, *9*, 1900072. [[CrossRef](#)]
28. Calizzi, M.; Mutschler, R.; Patelli, N.; Migliori, A.; Zhao, K.; Züttel, A. CO₂ hydrogenation over unsupported Fe-Co nanoalloy catalysts. *Nanomaterials* **2020**, *10*, 1360. [[CrossRef](#)]
29. Monshi, A.; Foroughi, M.R.; Monshi, M.R. Modified scherrer equation to estimate more accurately nano-crystallite size using XRD. *World J. Nano Sci. Eng.* **2012**, *2*, 154–160. [[CrossRef](#)]
30. Hatchard, T.D.; Dahn, J.R. In situ XRD and electrochemical study of the reaction of lithium with amorphous silicon. *J. Electrochem. Soc.* **2004**, *151*. [[CrossRef](#)]
31. Celebi, A.T.; Kirca, M.; Baykasoglu, C.; Mugan, A.; To, A.C. Tensile behavior of heat welded CNT network structures. *Comput. Mater. Sci.* **2014**, *88*, 14–21. [[CrossRef](#)]
32. Wang, H.W.; Skeldon, P.; Thompson, G.E. Thompson, Xps studies of mos 2 formation from ammonium tetrathiomolybdate solutions. *Surf. Coat. Technol.* **1997**, *91*, 200–207. [[CrossRef](#)]
33. Yang, H.; Zhang, C.; Gao, P.; Wang, H.; Li, X.; Zhong, L.; Wei, W.; Sun, Y. A review of the catalytic hydrogenation of carbon dioxide into value-added hydrocarbons. *Catal. Sci. Technol.* **2017**, *7*, 4580–4598. [[CrossRef](#)]

34. Sorribes, I.; Liu, L.C.; Corma, A. Nanolayered Co–Mo–S catalysts for the chemoselective hydrogenation of nitroarenes. *ACS Catal.* **2017**, *7*, 2698–2708. [[CrossRef](#)]
35. Wang, S.G.; Li, X.; Chen, Y.; Cai, X.J.; Yao, H.L.; Gao, W.; Zheng, Y.Y.; An, X.; Shi, J.L.; Chen, H.R. A facile one-pot synthesis of a two-dimensional MoS₂/Bi₂S₃ composite theranostic nanosystem for multi-modality tumor imaging and therapy. *Adv. Mater.* **2015**, *27*, 2775–2782. [[CrossRef](#)]
36. Liu, Z.L.; Peng, W.X.; Zare, Y.; Hui, D.; Rhee, K.Y. Predicting the electrical conductivity in polymer carbon nanotube nanocomposites based on the volume fractions and resistances of the nanoparticle, interphase, and tunneling regions in conductive. *RSC Adv.* **2018**, *8*, 19001–19010. [[CrossRef](#)]
37. Yang, P.; You, X.; Yi, J.H.; Fang, D.; Bao, R.; Shen, T.; Liu, Y.C.; Tao, J.; Li, C. Influence of dispersion state of carbon nanotubes on electrical conductivity of copper matrix composites. *J. Alloys Compd.* **2018**, *752*, 376–380. [[CrossRef](#)]
38. Albo, J.; Saez, A.; Sollagullon, J.; Irabien, A. Production of methanol from CO₂ electroreduction at Cu₂O and Cu₂O/ZnO-based electrodes in aqueous solution. *Appl. Catal. B Environ.* **2015**, *176*, 709–717. [[CrossRef](#)]
39. Albo, J.; Beobide, G.; Castano, P.; Irabien, A. Methanol electrosynthesis from CO₂ at Cu₂O/ZnO prompted by pyridine-based aqueous solutions. *J. CO₂ Util.* **2017**, *18*, 164–172. [[CrossRef](#)]
40. Chang, X.; Wang, T.; Zhao, Z.J.; Yang, P.; Greeley, J.; Mu, R.; Zhang, G.; Gong, Z.; Luo, Z.; Chen, J.; et al. Tuning Cu/Cu₂O interfaces for the reduction of carbon dioxide to methanol in aqueous solutions. *Angew. Chem.* **2018**, *130*, 15507. [[CrossRef](#)]
41. Jang, Y.J.; Jeong, I.; Lee, J.; Ko, M.J.; Lee, J.S. Unbiased sunlight-driven artificial photosynthesis of carbon monoxide from CO₂ using a ZnTe-based photocathode and a perovskite solar cell in tandem. *ACS Nano* **2016**, *10*, 6980–6987. [[CrossRef](#)] [[PubMed](#)]
42. Qiu, J.; Zeng, G.T.; Ha, M.; Ge, M.Y.; Lin, Y.J.; Hettick, M.; Hou, B.Y.; Alexandrova, A.N.; Javey, A.; Cronin, S.B. Artificial photosynthesis on TiO₂-passivated InP nanopillars. *Nano Lett.* **2015**, *15*, 6177–6181. [[CrossRef](#)] [[PubMed](#)]

Publisher's Note: MDPI stays neutral with regard to jurisdictional claims in published maps and institutional affiliations.



© 2020 by the authors. Licensee MDPI, Basel, Switzerland. This article is an open access article distributed under the terms and conditions of the Creative Commons Attribution (CC BY) license (<http://creativecommons.org/licenses/by/4.0/>).